FACULTY OF MATHEMATICS AND PHYSICS
Charles University

SUMMARY OF DOCTORAL THESIS

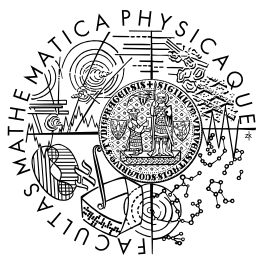Filip Kostka

Dynamic models of the earthquake source

Department of Geophysics

Supervisor of the doctoral thesis: doc. RNDr. František Gallovič, Ph.D.

Study programme: Physics

Study branch: Physics of the Earth and Planets

Prague 2022

AUTOREFERÁT DIZERTAČNÍ PRÁCE

Filip Kostka

Dynamické modely zemětřesného zdroje

Katedra geofyziky

Vedoucí dizertační práce: doc. RNDr. František Gallovič, Ph.D.

Studjiní program: Fyzika

Studijní obor: Fyzika Země a planet

Praha 2022

Dizertace byla vypracována na základě výsledků získaných v letech 2015-2021 během doktorandského studia na Katedře geofyziky MFF UK.

Dizertant:
Mgr. Filip Kostka
Katedra geofyziky MFF UK
V Holešovičkách 2, 180 00 Praha 8

Školitel:
doc. RNDr. František Gallovič, Ph.D.
Katedra geofyziky MFF UK
V Holešovičkách 2, 180 00 Praha 8

Oponenti:
Dr. Yoshihiro Kaneko
Department of Geophysics
Graduate School of Science, Kyoto University
Postal Code: 606-8502
Kitashirakawa, Oiwake-cho, Sakyo-ku, Kyoto, Japan

RNDr. Jan Burjánek, PhD.
Geofyzikální ústav Akademie věd, v. v. i.
Boční II/1401, 141 31 Praha 4

Předsedkyně oborové rady:
doc. RNDr. Hana Čížková, Ph.D.
Katedra geofyziky MFF UK
V Holešovičkách 2, 180 00 Praha 8

Obhajoba dizertace se koná dne 15.3.2022 v 9:00 hodin před komisí pro obhajoby dizertačních prací v oboru Fyzika Země a planet v budově MFF UK, Katedra geofyziky, V Holešovičkách 2, v místnosti A1132.

S dizertací je možno se seznámit v PGS MFF UK, Ke Karlovu 3, Praha 2.

Contents

1 Introduction

In the dynamic approach to earthquake modeling, the earthquake sources are described by the forces that govern their movement. As such, dynamic models are to be contrasted with kinematic (dislocation) models, which ignore the causative forces and directly prescribe the relative motion (slip) between tectonic fault surfaces. A great advantage of kinematic models is that they allow fast calculation of displacement outside of the fault. With suitable parametrization, they lead to linear problems and provide a more direct and transparent connection between slip and synthetic seismograms than dynamic models, which are non-linear and take more time to solve. But even though any kinematic model in an elastic medium has an associated surface force distribution, these distributions are often not realistic and violate reasonable assumptions such as continuity and causality.

The most common dynamic earthquake source models are those rooted in the field of fracture mechanics. Early studies modeled earthquakes as propagating ideally brittle cracks, assuming sudden release of stress behind the crack front. Even though such models can provide valid insights and approximate more realistic models in certain situations, they lead to infinite stresses and slip rates. They are also not consistent with laboratory and seismologic studies which show that the stress on the fault has a complicated dependence on slip, slip rate, and other field quantities.

These problems can be solved in the framework of cohesive fracture. Here, the spatial distribution of stress and slip rate on the fault is made finite and continuous by means of a suitably chosen constitutive law. This is a rule relating traction to other physical quantities, most notably the slip, the slip rate, the normal stress and position, but possibly also time, temperature, porosity, or certain abstractly defined state variables. The constitutive law represents the forces acting during the rupture process and it is mathematically posed as a boundary condition on the fault. As such, it allows describing fracture and friction in a unified manner. Coupling the constitutive law with continuum equations of motion in a volume surrounding the fault allows calculating the displacement everywhere in the volume, including the slip.

The problem of determining the correct constitutive law is crucial for earthquake physics and has been the subject of theoretical, laboratory, and field studies. The most prominent constitutive law used in dynamic modeling of fast rupture is the *linear slip-weakening law*. It is mainly used for simplicity and efficiency but captures the most dominant feature of fast rupture, the rapid decrease of traction with slip.

An important piece of the puzzle is the values of parameters of this constitutive law on seismic faults. Their extrapolation from laboratory experiments, typically conducted on scales much smaller than seismic faults and at low values of slip rate, is not straightforward. One method in which they can be uncovered is dynamic source inversion. Unlike the forward problem described in the previous paragraph, in which initial conditions and the constitutive law are used to obtain displacement on the ground, this is an inverse problem, which uses ground motion measurements (seismograms and/or GPS data) to infer the parameters of the constitutive law and the initial conditions on the fault.

However, the interpretation of the inversion results is not straightforward. The first issue is that neither the ground motion measurements nor the solutions of the forward problem are exact, due to, for example, seismogram errors, inaccuracies in the rheological model of the crust, imprecise geometry of the fault, numerical errors, etc. This leads to inaccuracy in the obtained model parameters. Another source of uncertainty is that a large (possibly infinite) number of models can fit seismic data equally well, which may lead to non-uniqueness of the inverse problem. A natural way to understand and quantify these uncertainties is to frame the inversion as a problem of Bayesian inference on the model parameters. In this approach, the result of the inversion is not a single model, but rather a joint probability density function on the space of model parameters. This function, called the *posterior probability density function*, quantitatively describes the plausibility of every model.

The second issue, inherent to every inverse method, is that the results are strongly affected by the starting assumptions, be they implicit or explicit. An important part of these is the prior assumptions about the model parameters. A key feature of Bayesian inverse methods is that these initial assumptions can, indeed must, be clearly formulated, in the form of the *prior probability density function*. However, another set of assumptions is that on the forward problem itself. What if inversions that assume a particular class of dynamic models tend to be biased toward certain values of the initial stress or frictional parameters, regardless of the seismic data? For example, the condition that a fracture propagates at all will cause the inversion to select or prefer a certain subset of the model space, depending on the assumed constitutive law, fault geometry, etc. Bias may also appear when we constrain the models in a way that is independent of the seismogram time series observed at the stations, e.g., by requiring that they produce a given moment magnitude. In the thesis, we present a Bayesian dynamic inversion method in which we try to separate the effects of different constraints on the resulting posterior probability density function. We do this by calculating and quantitatively comparing multiple intermediate probability density functions, each of which corresponds to adding progressively more information to the inversion. We apply the method to the 2017 M_w 6.3 Lesvos, Greece earthquake.

The fast rupture process that generates seismic waves – the co-seismic phase of rupture - is but one portion of dynamic earthquake source modeling. Another important component is the slow and often complicated evolution of slip and stress between the earthquakes, the so-called inter-seismic

phase. Unlike the first process, which is over in seconds to tens of seconds, the latter process may occur on the time scale of hundreds of years. Because of the vastly different time scales, it has been difficult to study the inter-seismic and the co-seismic phases in a unified manner. The most common constitutive law used to study the inter-seismic phase is the so-called *rate-and-state friction law*, a phenomenological frictional law derived from laboratory experiments conducted at low slip rates. The rate-and-state friction laws predict that under certain ideal conditions, faults undergo simply periodic seismic cycles, hosting large characteristic earthquakes separated by regular inter-seismic periods. However, when shear or normal stress on the fault is suddenly increased or decreased, the cycle is disturbed and the arrival of the next earthquake in the cycle is either hastened or delayed. In the thesis, we thoroughly examine the dependence of the earthquake occurrence time on the properties of the perturbation, in particular its timing during the cycle, and show that in some cases, a very large delay can be induced, even for a positive stress perturbation. We numerically demonstrate that this mechanism could have been the cause of the significant delay of the M_w 6 2004 earthquake observed on the Parkfield segment of the San Andreas fault.

1.1 Formulation of the dynamic source problem

The dynamic earthquake source problem dealt with in the thesis can be formulated in the framework of fracture mechanics.

Let $\Omega \subset \mathbb{R}^3$ represent a referential configuration of a linearly elastic body at time $t = 0$. Points in this referential body are labeled by $\boldsymbol{x}$. Let $\Gamma \subset \Omega$ be a fixed two-dimensional simple oriented surface (the *fault*). The displacement vector $\boldsymbol{u}(t, \boldsymbol{x})$ is assumed smooth on $\Omega \backslash \Gamma$, but allowed to be discontinuous on Γ. The discontinuity $\boldsymbol{s}$ of $\boldsymbol{u}$ across Γ is called *slip:*

$$s(t, \boldsymbol{\xi}) = \lim_{\epsilon \to 0}[\boldsymbol{u}(t, \boldsymbol{\xi} + \epsilon \boldsymbol{n}(\boldsymbol{\xi})) - \boldsymbol{u}(t, \boldsymbol{\xi} - \epsilon \boldsymbol{n}(\boldsymbol{\xi}))], \ \boldsymbol{\xi} \in \Gamma, \tag{1.1}$$

where $\boldsymbol{n}$ is a field of unit vectors normal to Γ.

We assume that the body is initially in static equilibrium and denote the initial Cauchy stress tensor by $\sigma^0(\boldsymbol{x})$. The incremental stress tensor $\tau(t, \boldsymbol{x})$ is defined as

$$\tau(t, \boldsymbol{x}) = \sigma(t, \boldsymbol{x}) - \sigma^0(\boldsymbol{x}). \tag{1.2}$$

In the absence of body forces and when the spatial derivatives of the deviatoric part of σ^0 are negligible, the equation of motion in the body, correct to first order in the gradient of $\boldsymbol{u}$, can be written as (Martinec, 2019, ch. 9.6):

$$\rho(\boldsymbol{x})\partial_{tt}u_i(t, \boldsymbol{x}) = \tau_{ij,j}(t, \boldsymbol{x}) \ \forall \boldsymbol{x} \in \Omega. \tag{1.3}$$

Under the approximation of linear elasticity, the stress increment is linearly related to the gradient of $\boldsymbol{u}$ through the fourth-order stiffness tensor c:

$$\tau_{ij}(t, \boldsymbol{x}) = c_{ijkl}(\boldsymbol{x})u_{k,l}(t, \boldsymbol{x}). \tag{1.4}$$

The classical elastodynamic problem consists of finding a displacement field $\boldsymbol{u}(t, \boldsymbol{x})$ that i) solves Eqs. (1.3)-(1.4), ii) satisfies the initial conditions $\boldsymbol{u}(0, \boldsymbol{x}) = \boldsymbol{u}_0(\boldsymbol{x})$ and $\partial_t \boldsymbol{u}(0, \boldsymbol{x}) = \boldsymbol{v}_0(\boldsymbol{x})$ for $\forall \boldsymbol{x} \in \Omega$, and iii) satisfies specified boundary conditions on $\partial\Omega$. In dynamic earthquake models, it is further required that *mixed boundary conditions* on Γ be satisfied. To define these conditions, the existence of a surface of fracture (crack) $\gamma(t) \subseteq \Gamma$ is postulated. The set $\gamma(t)$ may be prescribed in advance or it may spontaneously evolve according to a specified crack-propagation criterion. The mixed boundary conditions require that:

1. No slip occurs outside of $\gamma(t)$:
$$s(t, \boldsymbol{\xi}) = \boldsymbol{0} \ \forall \boldsymbol{\xi} \in \Gamma \backslash \gamma(t). \tag{1.5}$$

2. The traction field $\boldsymbol{T}$ within $\gamma(t)$ is constrained by a constitutive law of the form:

$$\boldsymbol{T}(t, \boldsymbol{\xi}) \in \mathcal{T}(t, \boldsymbol{\xi}, p_1(t, \boldsymbol{\xi}), p_2(t, \boldsymbol{\xi})..., p_n(t, \boldsymbol{\xi})) \ \forall \boldsymbol{\xi} \in \gamma(t). \tag{1.6}$$

Here, $\mathcal{T}(t, \boldsymbol{\xi}, p_1(t, \boldsymbol{\xi}), p_2(t, \boldsymbol{\xi})..., p_n(t, \boldsymbol{\xi}))$ is a set of admissible tractions and p_i are scalar or vector fields on the crack. The most important examples of p_i include the slip $\boldsymbol{s}$, slip rate $\dot{\boldsymbol{s}}$, normal stress

$$\sigma_n := \boldsymbol{T} \cdot \boldsymbol{n} = \boldsymbol{n} \cdot \sigma \cdot \boldsymbol{n}, \tag{1.7}$$

temperature, porosity, or abstract scalar variables that characterize the state of the sliding interface. Note that the constraint is imposed on the total traction, not only on the traction increment.

In the simplest case, $\mathcal{T} \equiv \{\boldsymbol{T_d}\}$, where $\boldsymbol{T_d}$ is a constant vector. This corresponds to a special case of brittle fracture mechanics. In the part of the thesis in which we present original research, we instead work with two types of cohesive constitutive laws: the slip-weakening law and the rate-and-state law. Both of these constitutive laws are assumed to take the form:

$$\mathcal{T}(t, \boldsymbol{\xi}, ...) = \left\{ \boldsymbol{T} : \boldsymbol{T}_s = -F(t, \boldsymbol{\xi}, ...) \frac{\dot{\boldsymbol{s}}_s(t, \boldsymbol{\xi})}{\|\dot{\boldsymbol{s}}_s(t, \boldsymbol{\xi})\|} \right\} \ \forall \boldsymbol{\xi} \in \gamma(t) : \dot{\boldsymbol{s}}_s(t, \boldsymbol{\xi}) \neq \boldsymbol{0}, \tag{1.8}$$

where the function F is called *shear strength*, the ellipses represent the dependence on the fields $p_1(t, \boldsymbol{\xi}), ..., p_n(t, \boldsymbol{\xi})$,

$$\boldsymbol{T}_s := \boldsymbol{T} - \sigma_n \boldsymbol{n} = \boldsymbol{T} - (\boldsymbol{n} \cdot \boldsymbol{T})\boldsymbol{n} \tag{1.9}$$

is the shear traction, and

$$\boldsymbol{s}_s := \boldsymbol{s} - (\boldsymbol{n} \cdot \boldsymbol{s})\boldsymbol{n} \tag{1.10}$$

is the shear slip. This means that during slip, the shear traction points in the direction opposite the slip rate.

When the slip rate $\dot{\boldsymbol{s}}_s = \boldsymbol{0}$, only the condition that the magnitude of $\boldsymbol{T}_s$ is bounded by the shear strength is imposed:

$$\mathcal{T}(t, \boldsymbol{\xi}, ...) = \{\boldsymbol{T} : \|\boldsymbol{T_s}(t, \boldsymbol{\xi})\| \leq F(t, \boldsymbol{\xi}, ...)\} \ \forall \boldsymbol{\xi} \in \gamma(t) : \dot{\boldsymbol{s}}_s(t, \boldsymbol{\xi}) = \boldsymbol{0}. \tag{1.11}$$

The linear slip-weakening law and the rate-and-state law are summarized below.

1.1.1 Linear slip-weakening law

In the *linear slip-weakening* law, introduced formally by Ida (1972) and first utilized for rupture modeling by Andrews (1976a,b), the expression for the shear strength reads

$$F(s) := \begin{cases} (T_u - T_d)(1 - s/D_c) + T_d & \text{for } 0 \leq s \leq D_c \\ T_d & \text{for } s > D_c \end{cases}.$$

(1.12)

Here, T_u is the yield strength, T_d is dynamic friction, D_c is the characteristic slip-weakening distance and s is a scalar variable that characterizes slip (see below). All of these quantities may vary with space and time.

Two versions of the law are commonly used. In one version, the argument s represents the magnitude of slip $\|\boldsymbol{s}\|$. In the other version, which is assumed in the thesis, s represents the *slip-path length* $\mathfrak{s}$:

$$\mathfrak{s}(t, \boldsymbol{\xi}) = \int_0^t |\dot{\boldsymbol{s}}(t', \boldsymbol{\xi})| dt'.$$

(1.13)

In the latter version, if the slip vector makes a round trip along a closed curve, the resulting shear strength is weaker than the initial strength, which is physically plausible. In the former version, the shear strengths would be identical. See Bizzarri (2014) for a comparison.

The linear slip-weakening law is one of the most common laws employed in earthquake modeling, even though it has no proper empirical support in laboratory experiments. This is mainly because it is simple to use and captures the observed decrease of traction at larger values of slip (Hirose, 2005; Ohnaka, 2013). A potential disadvantage of slip-dependent laws is that they do not allow (without further modifications, see Aochi & Matsu'ura, 2002; Bizzarri, 2012) for fault restrengthening and modeling long-term evolution of faults (e.g., seismic cycles). Therefore, they are mostly used for modeling fast fast, short-term rupture on the time scale of seconds to tens of seconds. For a review of important properties of linear slip-weakening models, see chapter 3 of the thesis.

1.1.2 Rate-and-state dependent friction laws

The rate-and-state (RS) friction laws were postulated to explain the behavior of friction acting on precut rock surfaces mutually sliding at low values of slip rate ($\lesssim 1$ mm/s). Two types of experiments were particularly important for their establishment. In the *velocity stepping* tests (e.g., Dieterich, 1979; Marone et al., 1990; Bohloli et al., 2020) a rock specimen is sheared under externally imposed constant normal stress and slip rate. After some time, the shear stress reaches a steady-state value. When the imposed slip rate is abruptly changed, the coefficient of friction jumps in proportion to the difference in logarithms of the new and the old slip rate. After the jump, it is observed that the shear

stress starts evolving towards a new steady-state value that depends on the new slip rate. The second type of founding experiments are the *slide-hold-slide* tests (e.g., Dieterich, 1972; Beeler et al., 1994; Marone & Saffer, 2015), in which a steadily sliding block is (almost) stopped for some time Δt and then forced to slide again. For a wide variety of materials, it was observed that the "static" coefficient of friction (the traction at the onset of sliding) increases approximately in proportion to the logarithm of Δt. To model the described behavior, it was proposed (Dieterich 1979; Ruina 1983; in a somewhat different but equivalent form) to use the following constitutive law (denoting $V := \|\dot{\boldsymbol{s}}\|$):

$$F(\sigma_n, V, \theta) = \sigma_n f(V, \theta), \tag{1.14}$$

with the *coefficient of friction* $f(V, \theta)$ given by:

$$f(V, \theta) = f^* + a \ln \frac{V}{V^*} + b \ln \frac{V^* \theta}{L}, \tag{1.15}$$

where f^*, V^*, a, b and L are positive (and possibly position dependent) parameters. The first term of Eq. (1.15), f^*, is simply a referential value of the coefficient of friction such that $\sigma_n f^*$ is the friction measured when two surfaces are steadily sliding over another at the constant referential slip rate V^*. The second term models the direct velocity (slip rate) effect observed in the velocity-stepping tests. The third term describes the evolutionary behavior - the gradual increase of static friction and the relaxation to the steady-state - which cannot be explained by a purely rate-dependent law. They are encoded in the *state variable* $\theta(t)$ which figures in the third term. The state variable evolves according to a prescribed first-order differential equation. In the thesis, we assume that the state variable evolves with time according to the so-called *aging* law (Ruina, 1980, 1983):

$$\frac{d\theta}{dt} = 1 - \frac{V\theta}{L}. \tag{1.16}$$

A great advantage of the RS laws is that they allow modeling many features of the fault behavior, such as nucleation, propagation, arrest, healing, triggering, aseismic creep, slow earthquakes, etc., in a unified manner (see chapter 4 of the thesis for a brief review), which is very convenient for numerical modeling. On the other hand, the scope of validity of the RS friction laws is limited by the fact that the experiments that motivated them were performed under small slip rates, in the range of $\approx 10^{-8} - 10^{-3}$ m/s. This is several orders lower than co-seismic slip rates, which may be as large as $\approx 10^1$ m/s (McGarr, 2003). In addition, at seismic speeds, the RS laws behave similarly to the linear slip-weakening law, which is simpler to use. Therefore, the RS laws are better suited to simulate quasi-static and long-term evolution of faults, although modifications have been developed that take large velocity effects effect into account (Ampuero & Ben-Zion, 2008; Gabriel et al., 2012; Zelst et al., 2019; etc.).

2 Static Coulomb stress load on a three-dimensional rate-and-state fault: Possible explanation of the anomalous delay of the 2004 Parkfield earthquake

This summary is based on chapter 5 of the thesis, which is itself based on a paper published as Kostka & Gallovič (2016).

2.1 Introduction and method

Many earthquake faults undergo a quasi-periodic seismic cycle, where long-term tectonic loading is released in a form of characteristic earthquakes (Wesnousky, 1994; Stirling et al., 1996). The characteristic earthquakes are believed to be large enough to dominate the seismic moment release and substantially reduce the average stress. However, this simple behavior is complicated by at least two facts. First, real faults are characterized by frictional and geometric complexities that result in heterogeneity in the stress redistribution along the fault, altering the occurrence of the characteristic earthquakes. Second, the faults do not exist individually, and thus the earthquake occurrence is affected by external stress perturbations due to, for example, slip on nearby faults.

In the thesis, we extend previous studies on the effect of these perturbations on seismic cycles (e.g., Kato & Hirasawa, 2000; Perfettini et al., 2003; Kato, 2004; Kuroki et al., 2004; Liu & Rice, 2007; Gallovič, 2008, etc.) by performing a detailed systematic analysis of the clock advance on a 3-D rate-and-state strike-slip fault model. We investigate the dependence of the clock advance on the onset time of the stress load, its amplitude, area, and place of application. We point out that many of the observed dependencies are related to 3-D effects of the slip velocity/stress evolution and thus cannot be modeled by a simple spring slider model (in accordance with earlier studies). We find that in some cases the advanced event may rupture only a portion of the fault (having a smaller magnitude), causing a significant clock delay of the next main shock. We also suggest that a related mechanism may have played a role in the surprisingly long delay of the 2004 M_w 6 Parkfield earthquake (Bakun

et al., 2005).

We use a model of a planar strike-slip two-dimensional square vertical fault of dimensions $R \times R$ embedded in a 3-D homogeneous isotropic half-space and discretized into square cells. The shear traction τ_i on $i-th$ cell is given by the rate-and-state friction law (1.14)-(1.16). This traction must be balanced by both elastic and radiative contributions, as well as the external shear stress perturbations $\Delta\tau_i(t)$:

$$\tau_i(t) = \sum_j K_{ij}\left(s_j(t) - V_{pl}t\right) - \frac{\mu}{2\beta}V_i(t) + \Delta\tau_i(t), \qquad (2.1)$$

where $s_j(t)$ is the slip on the cell j at time t, V_{pl} is the constant driving plate velocity, μ is the elastic shear modulus, and β is the S-wave velocity. Kernel K_{ij} of elastic interactions represents the static stress induced on cell i by unit slip on cell j, which we evaluate using analytical solutions by Okada (1992). The middle term on the right-hand side of Eq. (2.1) corresponds to the (standardly added) viscous term introduced by Rice (1993), also called the radiation damping term, which approximates the effect of seismic wave radiation. Outside the model fault zone, continuous stable sliding is assumed ($V = V_{pl}$).

We pick a reference time t_r after several earthquake cycles. In absence of external perturbations, an event occurs at time $t_u > t_r$. At time t_0 such that $t_u > t_0 > t_r$, we apply, to selected parts of the fault, an external stress perturbation that rapidly (but continuously) increases shear traction by $\Delta\tau_i = \Delta$CS. As a result of the stress perturbation, one or more events will nucleate at hypocentral times which will generally differ from t_u. The seismic magnitudes of the events will also generally differ from the unperturbed case. The clock advance CA is defined as

$$\text{CA} = t_u - t_p, \qquad (2.2)$$

where t_p refers either to the occurrence time of the subsequent event regardless of its magnitude (*magnitude-unconstrained* CA), or the subsequent event with magnitude larger than the threshold magnitude M_{tr} (*magnitude-constrained* CA). When CA is negative, we also refer to its absolute value as clock delay. In the thesis, we explore the dependence of CA on t_0, ΔCS and the area and location of the stress perturbation.

2.2 Results

2.2.1 Homogeneous model

In this subsection, we consider a homogeneous fault in the velocity-weakening regime ($a-b = 0.004 > 0$), composed of 128×128 cells and embedded in a homogeneous elastic space with constant normal

stress σ. At the beginning of the simulation, the model is initiated by setting slip velocities to twice the plate velocity V_{pl} on the whole fault. After one or two earthquakes, the fault reaches a stable cycle of repeating events of magnitude $M_w = 6.9$.

We set the origin of the time coordinate to $t_r = 733.0$ years since the start of the simulation, which corresponds to the beginning of the eighth earthquake cycle. To see the effect of the stress load on the clock advance (CA), we run the earthquake cycle 500 times, each time applying the shear stress increase or decrease of magnitude $\Delta CS = \pm 0.01~\sigma$ (approximately 14% of the main shock stress drop) to the whole fault at a different onset time t_0 and measure the resulting CA. Fig. 2.1 shows the dependence of the magnitude-constrained ($M_w > M_{tr} = 6$) and the magnitude-unconstrained CA on the load time t_0 for both positive and negative loads.

The magnitude-unconstrained CA curves in Fig. 2.1 can be separated into three to four phases: static, increasing, and decreasing. The fourth phase, corresponding to instantaneous triggering, is present only in the case of positive stress load. The increasing and decreasing phases are jointly referred to as the oscillatory phase of CA. Such behavior of the (unconstrained) CA was first observed by Perfettini et al. (2003) and later by Gallovič (2008) on 2-D and 3-D rate-and-state faults, respectively. Here we analyze the behavior of the CA in more detail.

During the static phase, CA is a constant independent of t_0. In each decreasing phase, CA decreases approximately linearly, with a slope close to -1. This means that events occur after approximately constant time intervals from the CS load application. In the static and decreasing periods, the subsequent earthquake corresponds to a system-size event with magnitudes ranging from 6.5 to 7. This means that the magnitude-constrained and magnitude-unconstrained CA curves coincide (see Fig. 2.1). However, the situation is more complex in the increasing phase, where the smooth magnitude-unconstrained CA is related to the occurrence of events with magnitudes between 3.5 and 6 (see Fig. 2.1). In the magnitude-constrained case, i.e., when considering the occurrence of the system-size event, CA is characterized by abrupt changes with significant values of clock delay. We note that the intervals of t_0 associated with such clock delays are rather short, 1.3 years on average in the present example. Nevertheless, since there are six such intervals within the earthquake cycle (with average time spacing of 7.0 years), they altogether amount to 7.6 years, which corresponds to 8.5% of the whole cycle.

To better understand the behavior of the CA, we analyze the evolution of slip velocities on the fault after the stress load. Fig. 2.2 shows maximum velocity as a function of time for several examples of (positive) stress onset times t_0. In Fig. 2.3a we plot slip velocities at five different equidistant points located in the middle width of the fault. Immediately after the stress load, the slip velocities increase at the affected cells. For a simple spring slider model, one can derive an approximate formula for the change of velocity following Coulomb stress steps ΔCS (e.g., Perfettini et al. 2003). The formula predicts that the response to the stress step depends not only on its amplitude ΔCS (exponentially)
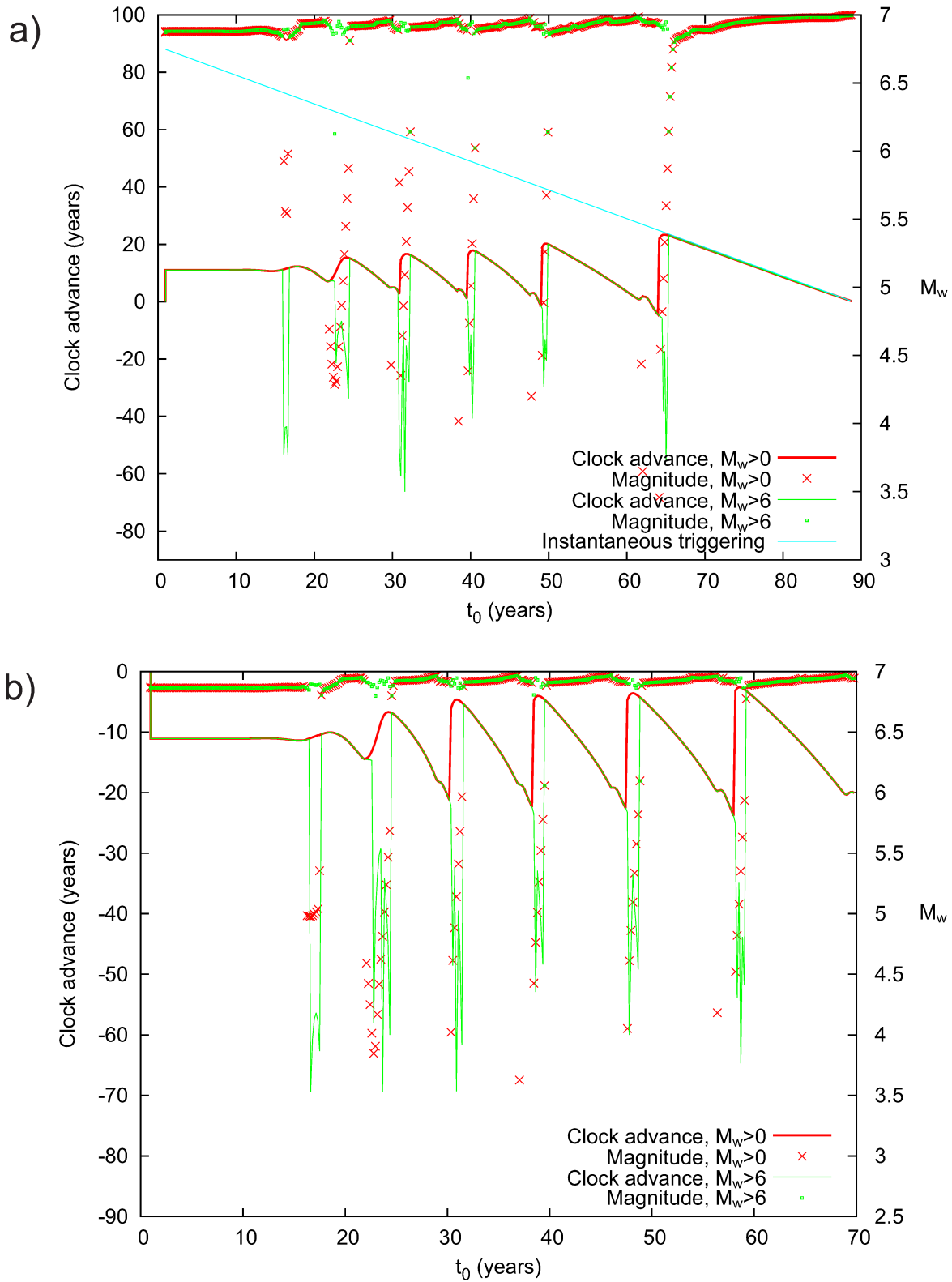
Figure 2.1: Clock advance CA (lines, left axes) and magnitude of the triggered events (symbols, right axes) as functions of stress load onset time t_0 for a) positive and b) negative loads. The red lines represent CA corresponding to the very first subsequent (triggered) event, regardless of its magnitude. The green lines correspond to CA of the first subsequent event with a magnitude larger than 6 (so-called magnitude-constrained CA). Note that the two curves depart only in the intervals of increasing CA, where the system-size events are significantly delayed for both the load and unload. The blue line corresponds to instantaneous triggering.

but also (linearly) on the slip velocity at the time of stress load. During the earthquake cycle, the slip velocities increase inward from the borders of the asperity from values corresponding to the locked fault to values corresponding to a creeping ($\approx V_{pl}$) fault, which differ by approximately 4 orders of magnitude. Therefore, the effect of the load is the most significant when applied to the creeping portion of the fault. For example, Fig. 2.3a demonstrates that only the creeping parts of the fault at the fault edge start to oscillate after the stress load. This response then in turn alters the stress field, which may lead to destabilization of the fault.

In particular, when the stress load is applied early after an event, the initial velocity jump is relatively small, because the fault is locked almost everywhere. In such a case the resulting slip velocity perturbations are relatively weak and get damped after a relatively short time (see Fig. 2.2a). Nevertheless, the overall velocity (and thus stress) increase remains stored in the system, leading to the observed independence of the CA on t_0 in the constant CA phase (see Fig. 2.1).

During the oscillatory phase of CA, the initial velocity jump results in quasi-periodic oscillations in maximum slip velocity, which do not get damped. Depending on the timing of the CS load, one of the episodic slip velocity increases, taking place close to the occurrence of the regular event, can either trigger the system-size event or fail in doing so. The former case would correspond to the decaying part of the CA curve (see Fig. 2.1), while the latter case would correspond to the increasing part of the magnitude-unconstrained CA curve. The failed events can release a significant part of the accumulated stress on the fault and the system-size event may thus get delayed by a significant fraction of the unperturbed earthquake cycle duration. A similar example of such failed nucleation is shown in Fig. 2.3b for a shear stress perturbation of amplitude $+0.01\sigma$ applied to the fault edge at $t_0 = 39.0$ years.

2.2.2 Possible Explanation of the Anomalous Delay of the Parkfield Earthquake

Our study is to be understood as a qualitative analysis of conceptual fault behavior after being perturbed by a stress load or unload. Nevertheless, the observed significant clock delays, occurring when the stress (un)load is applied at specific periods within the seismic cycle, call for comparisons with real fault observations. A perfect candidate is the locked Parkfield segment of the SAF. This fault is well known for its quasi-periodic occurrence of $M_w \approx 6$ events with a mean interval of about 22 years (see Fig. 5.8a in the thesis). The striking similarity of waveforms recorded in the 1922, 1934, and 1966 events suggests that the ruptured area of the fault is similar for all those events (Bakun et al., 2005). After the 1966 earthquake, the next M_w 6 event was anticipated to take place between 1988 and 1993. Interestingly, the event occurred as late as 2004, being delayed by approximately 15 years. The reason for this exceptional delay, representing a significant portion of the whole seismic cycle, remains enigmatic. Here we link it with the perturbation of the stress field by two nearby strong
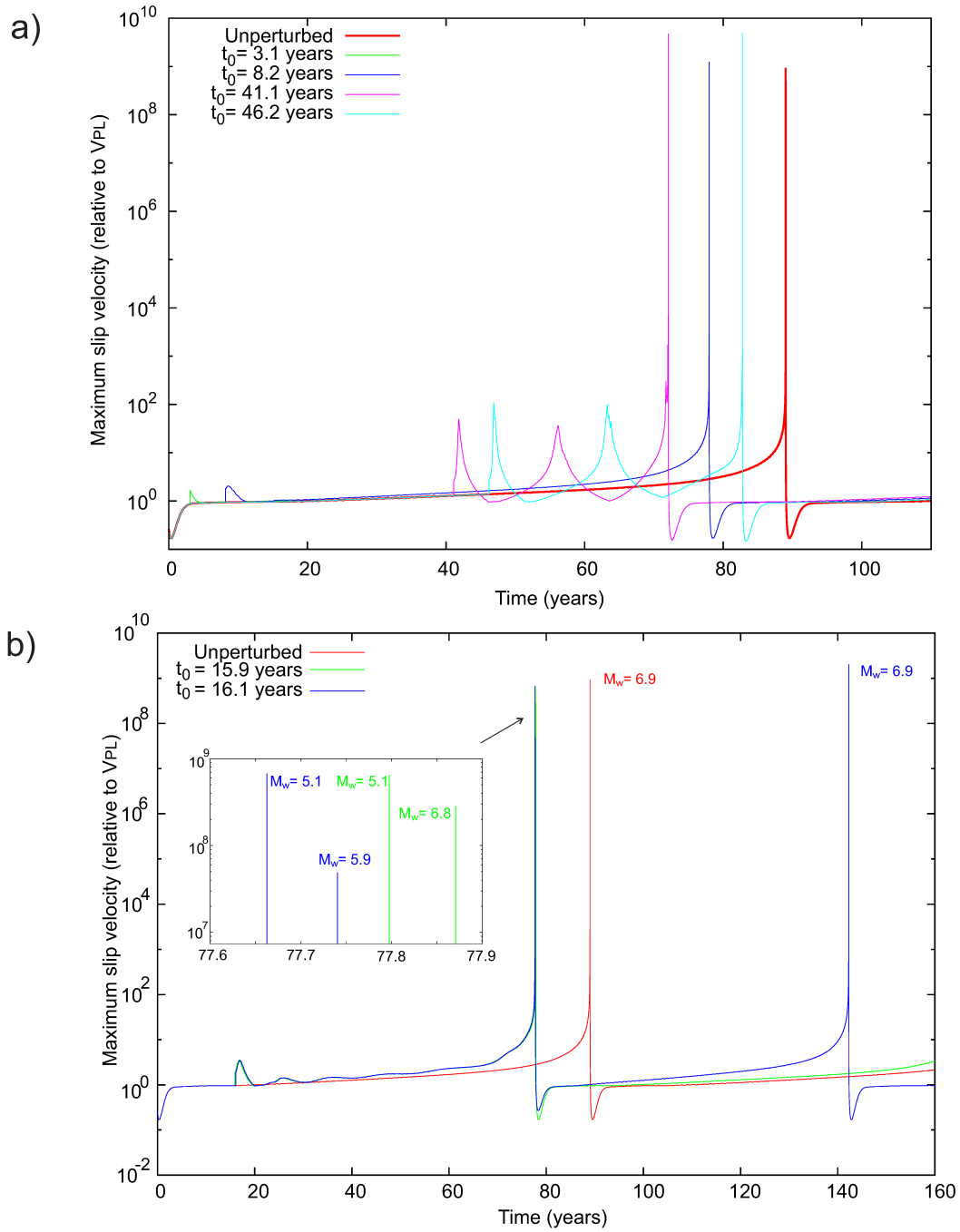
Figure 2.2: a) Evolution of the maximum slip velocities over the fault for selected stress loading times t_0 (see legend), corresponding to various parts of the CA plot in Fig. 2.1a. Loading times of 3.1 and 8.2 years correspond to the flat phase of the CA (see Fig. 2.1a). Loading times of 41.1 and 46.2 years were selected from the period of the CA decrease in Fig. 2.1a. The evolution of the slip velocities at five points for the case of loading at 41.1 years (here in magenta) is shown in Fig. 2.3a. b) The evolution of maximum slip velocities for two scenarios with t_0 only 2 months apart, at the boundary between the decreasing interval of the CA and the clock delay interval (Fig. 2.1a). Until the occurrence of the first smaller event, the evolution of the maximum slip velocities is very similar. Nevertheless, while for the smaller t_0, the first event is followed by a (clock advanced) system-size rupture of $M_w = 6.8$, for the larger t_0, the second event fails to rupture the whole fault (thus having smaller magnitude), even though its maximum slip velocity is larger than for the main shock triggered in the case of the smaller t_0. The whole fault is then ruptured 65 years later.
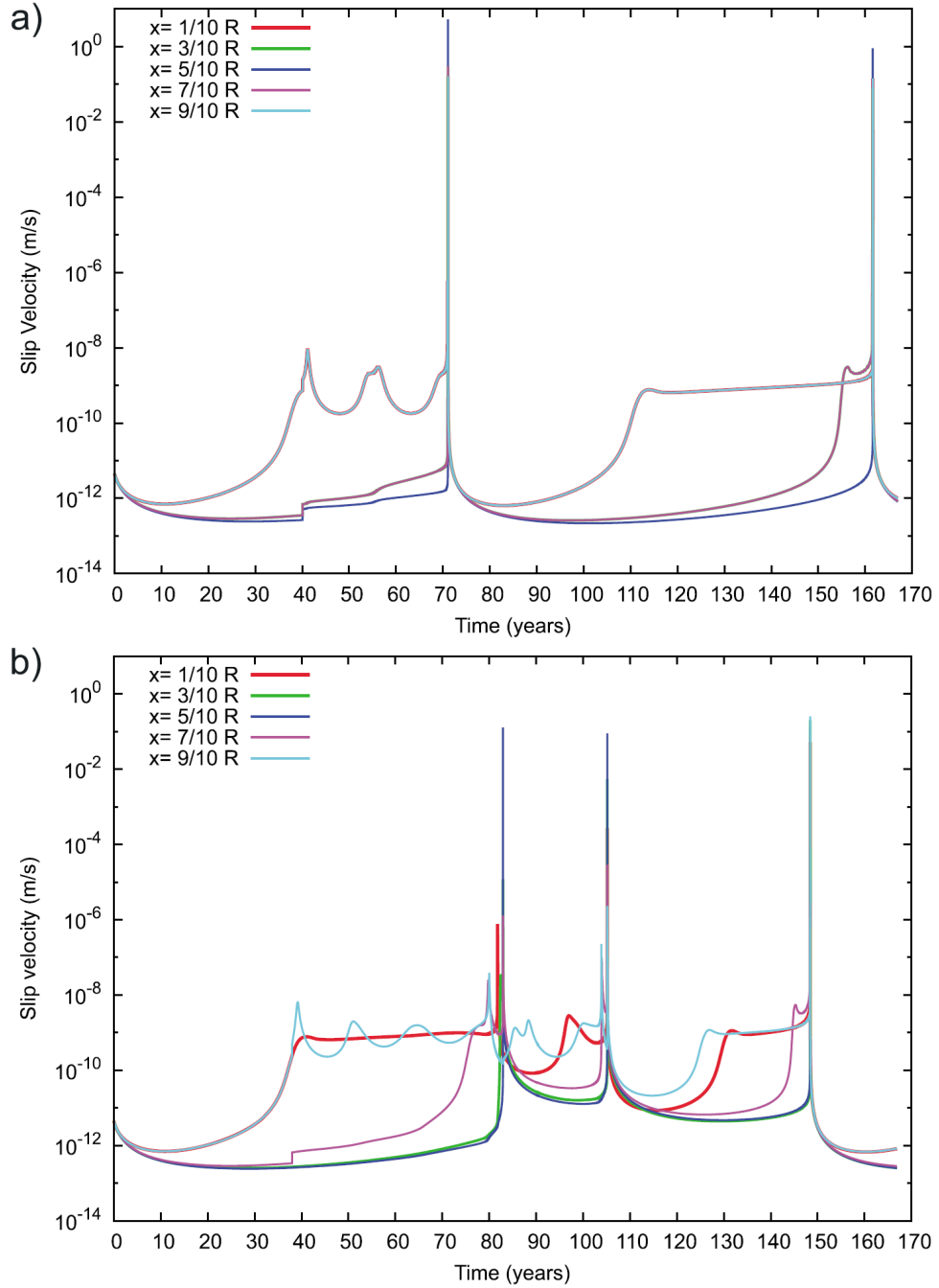
Figure 2.3: a) Evolution of slip velocities at five equidistant points along the middle horizontal cross-section of the fault (see legend) assuming a shear stress perturbation of amplitude $+0.01\sigma$ applied to the whole fault at $t_0 = 41.1$ years. The curves corresponding to the opposite sides of the fault overlap due to the symmetry of the model and the perturbation. Note the slow-slip oscillations at the edges of the fault. After the whole fault has been ruptured, it starts evolving in the same way as the unperturbed fault. b) Evolution of slip velocities at the same points as in a) when a shear stress perturbation of the same amplitude is applied to the edge of the fault at $t_0 = 39.0$ years. In this case, the oscillations are present only at the side of the fault affected by the stress increase. At 84 years only the center of the fault reaches seismic velocities, resulting in an event of magnitude 4.9. It is followed at 106 years by another event of magnitude 5.3, which ruptures a larger area. Eventually, the whole fault ruptures at 149 years, causing an event of magnitude 6.9 (equal to the original unperturbed magnitude), which is thus delayed by 60 years.

earthquakes that occurred northeast of the Parkfield section of SAF in 1983, M_w 6.5 Coalinga and M_w 6.0 Nuñez. Barbot et al. (2012) developed a rate-and-state dynamic model of the seismic cycle of the Parkfield segment of SAF. The authors replicated basic characteristics of the cycle including the swap of hypocenters of the 1966 and 2004 events. Nevertheless, they did not explain the anomalous delay of the latter event. Although they neglected the external unloading due to the nearby 1983 Coalinga-Nuñez events, the authors also raised the possibility that the delay of the 2004 M_w 6.0 Parkfield event may have been at least partially caused by smaller earthquakes occurring from 1993 to 1994, being perhaps a series of arrested M_w 6 nucleations.

To support this hypothesis, we consider a fault model with conditions closer to the properties of the Parkfield segment, following Barbot et al. (2012). In particular, we assume a strike-slip model with dimensions of 36 km × 18 km, which covers both seismogenic and aseismic parts of the SAF. For the sake of computational efficiency, we simplify the distribution of frictional parameters of Barbot et al. (2012), removing small seismogenic patches and using a simple rectangular seismogenic zone of 24 × 4 km (see Figures 2.4a and 2.4b).

After initialization, the fault quickly settles into a periodic regime with a period of 20.4 years. We apply a negative Coulomb stress change of 0.6 MPa to the velocity-weakening zone at 130 equidistant onset times t_0. The resulting dependence of both magnitude-constrained and magnitude-unconstrained CA on t_0 is shown in Fig. 2.4d, which is analogous to Fig. 2.1. We observe three intervals of significant clock delay. As in the homogeneous model, the large earthquake is delayed by one or two preceding smaller events. Their hypocenters generally differ from that of the main shock; in most cases, the main shock hypocenter is located closer to the edges of the velocity-weakening area. The stress perturbations also generate creep episodes with irregularly spaced peaks in slip velocity with intervals ranging between 0.4 and 3 years, i.e. covering the 2 year period of the repeating microearthquakes observed at Parkfield (Nadeau & McEvilly 1999, 2004). Nevertheless, we stress that the qualitative behavior of the fault is quite sensitive to variations of the model parameters. For example, no significant delays appear when considering a purely rectangular velocity-weakening zone. More comprehensive modeling of the Parkfield segment that would explain the fault behavior in full detail is left for further study.

Our results support the hypothesis of Barbot et al. (2012), suggesting that the stress unload due to the 1983 Coalinga-Nuñez earthquakes took place during a specific phase of the Parkfield seismic cycle (corresponding to the increasing phase of the CA curve; see Fig. 2.1). This resulted in the failure of the $\approx M_w$ 4.9 events from 1993 to 1994 to rupture the whole fault. Instead, they significantly delayed the 2004 M_w 6 main shock. We note that this proposed mechanism is not unique. For example, simulations by Ben-Zion et al. (1993) showed that accounting for viscoelasticity below the brittle crust can also produce a delay of the 2004 M_w 6 Parkfield earthquake; for some parameters, their calculations predicted the next Parkfield earthquake to occur in the time interval 1995 ± 11, which includes 2004.
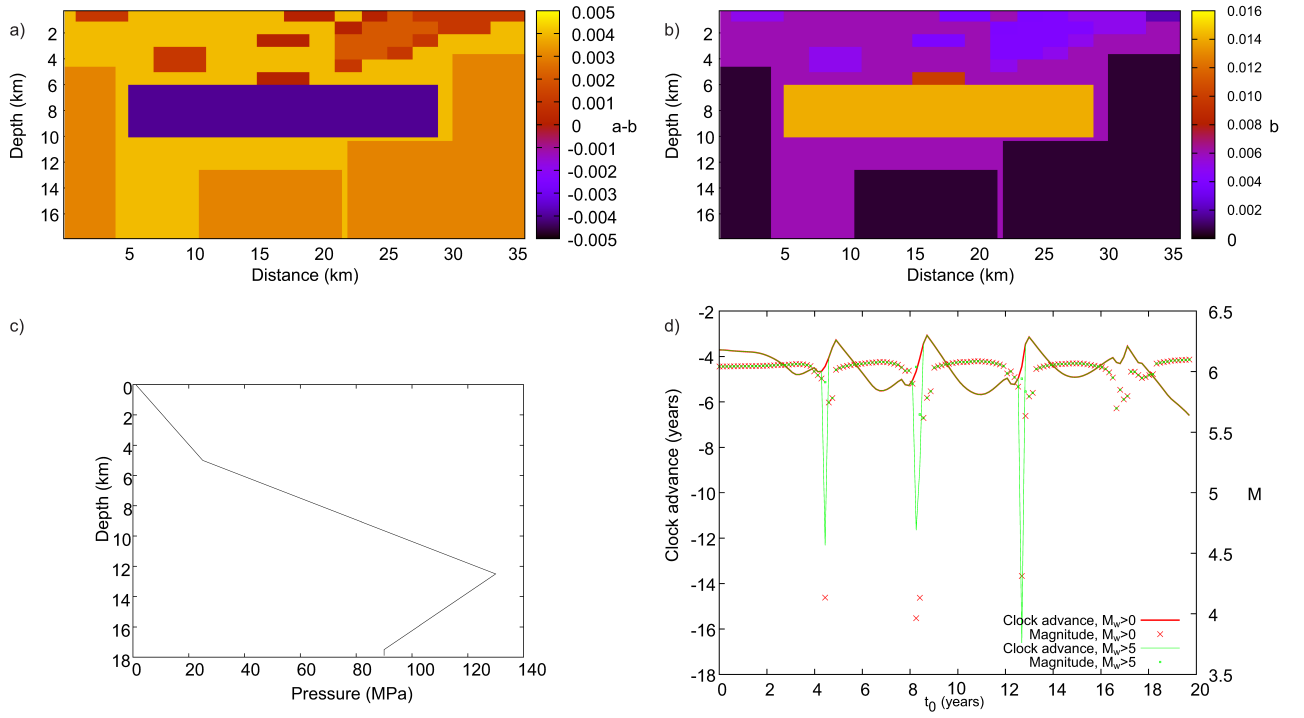
Figure 2.4: Parameters and the results for our model of the Parkfield fault segment. The parameters are simplified after Barbot et al. (2012) a) The spatial distribution of friction parameter $a-b$. The blue area corresponds to the velocity-weakening zone. b) The spatial distribution of friction parameter b. c) Depth dependence of the effective normal stress d) The dependence of the clock advance CA and magnitude of the triggered events as a function of stress load onset time t_0. We apply a negative Coulomb stress change on the velocity-weakening zone. The figure is analogous to Fig. 2.1. Note the significant time delays of the system-size ($M_w \approx 6$) events, which are preceded by $M_w < 5$ events, within the three intervals of load time t_0.

3 Assessing the role of selected constraints in Bayesian dynamic source inversion: Application to the 2017 M_w 6.3 Lesvos earthquake

This summary is based on chapter 6 of the thesis, which is itself based on a paper published as Kostka et al. (2022).

3.1 Introduction and method

Dynamic inversions of earthquake rupture aim at finding parameters governing frictional and stress conditions on a fault. This can be done in two ways. In the first approach, the stress on the fault is calculated from the history of slip obtained via inversion for a kinematic model, and the two fields are then used to estimate parameters of the constitutive law relating slip and friction (e.g. Fukuyama & Mikumo, 1993; Ide & Takeo, 1997; Pulido & Irikura, 2000; Peyrat et al., 2001; Tinti et al., 2005; Burjánek & Zahradník, 2007). A more recent approach, used here, is the fully dynamic inversion (e.g. Peyrat & Olsen, 2004; Di Carli et al., 2010; Ruiz & Madariaga, 2011, 2013; Díaz-Mojica et al., 2014; Twardzik et al., 2014; Herrera et al., 2017; Gallovič et al., 2019a,b; Mirwald et al., 2019; Gallovič et al., 2020). In this approach, simulations in which the elastodynamic equation is coupled with the constitutive law are used and the parameters describing the law and the initial stress on the fault are searched directly. The history of slip during the rupture is obtained as a by-product and it is guaranteed to be consistent with physical laws. Solving a fully dynamic inversion problem thus solves an associated kinematic inversion problem. In addition, dynamic inversions also permit interpretation of the earthquake properties in terms of physics. This is crucial for understanding processes of rupture nucleation, propagation, and arrest, eventually enabling realistic simulations of near-source ground motions (e.g. Aochi & Ulrich, 2015).

The solutions of dynamic inversions are non-unique and it is desirable to describe their uncertainty (Ruiz & Madariaga, 2013; Gallovič et al., 2019a,b). These facts motivate casting the problem in a

probabilistic, Bayesian framework and expressing the information about model parameters in the form of a joint *posterior probability density function*. This function provides a formal basis for analyzing uncertainties of model parameters and their trade-offs. Another advantage of the Bayesian framework is that it enables researchers to clearly formulate their prior assumptions (in the form of the *prior probability density function*) and to identify how they affect the resulting inference of model parameters.

However, interpreting the inversions results is difficult because it is not clear which constraints are responsible for the appearance of particular features. We investigate this issue by using progressively more information to update the prior probality distribution $\rho_{pr}(\boldsymbol{m})$ on model parameters $\boldsymbol{m}$ to calculate three posterior distributions. For the first posterior distribution $\rho_0(\boldsymbol{m})$, we use only the constraint that the rupture breaks at least twice the area of the nucleation zone and lasts more than 1 second. This rupture condition removes uninteresting models that produce negligible wave radiation. For the second distribution, $\rho_1(\boldsymbol{m})$, we add a constraint on the moment magnitude. The resulting distribution will characterize models with mechanisms and magnitude similar to the one from the moment tensor inversion, regardless of the observed waveforms. For the final posterior distribution, $\rho_2(\boldsymbol{m})$ we use both moment magnitude and waveforms observed at near-regional seismic stations.

The appropriate form of the update from the prior to the posterior distributions is given by *Bayes' formula*:

$$\rho(\boldsymbol{m}|\boldsymbol{c}) = kL(\boldsymbol{m}|\boldsymbol{c})\rho_{pr}(\boldsymbol{m}). \tag{3.1}$$

Here, $\boldsymbol{c}$ is a constraint (e.g., the approximate value of the scalar seismic moment or waveform data from seismic stations),

$$L(\boldsymbol{m}|\boldsymbol{c}) = \rho(\boldsymbol{c}|\boldsymbol{m}) \tag{3.2}$$

is the *likelihood function*, which represents the probability density function of $\boldsymbol{c}$ given that the true model parameters are equal to $\boldsymbol{m}$, and k is a normalizing constant such that $\rho(\boldsymbol{m}|\boldsymbol{c})$ integrates to 1.

We sample the distributions with a) a random number generator, discarding models that do not fit prescribed conditions (for distributions ρ_{pr} and ρ_0) and b) the Parallel Tempering Markov Chain Monte Carlo algorithm (for distributions ρ_1 and ρ_2, see Swendsen & Wang, 1986, Sambridge, 2013). We then use the obtained random samples to estimate the probality density functions using the Kernel density estimation (KDE) technique (Zambom & Dias, 2013). Details about the prior distribution and the assumed likelihood functions, as well as the used sampling and estimation techniques can be found in subsection 6.2.3 of the dissertation.

Comparing the three posterior distributions allows us to separate features that are determined by the rupture condition, those determined by magnitude, and those determined by waveforms. To compare the information contained in ρ_{pr}, ρ_0, ρ_1 and ρ_2, we measure the mutual dissimilarity of their 1-D marginal distributions for each parameter in terms of the Hellinger distance H (Shemyakin,

2014):

$$H_{i,j} = \left(1 - \int_{\mathbb{R}} \sqrt{\rho_i(x)\rho_j(x)}dx \right)^{1/2}. \tag{3.3}$$

To assess the reduction in uncertainty associated with each update, we also calculate the quantity rHDR$_{i,j}$, which is the ratio of the sizes of 68 % highest density regions of ρ_j and of ρ_i.

The distribution of friction and initial stress on the fault is defined by a single 12-parameter elliptic patch model Ruiz & Madariaga, 2011, 2013; Díaz-Mojica et al., 2014; Herrera et al., 2017 governed by the linear-slip weakening law (Eq. 1.12), see Fig. 3.1 and its description for more details. The forward problem consists of dynamic rupture simulation and calculation of synthetic waveforms in a layered isotropic medium. For the former, we use the Fortran code FD3D_TSN (Premus et al., 2020), which employs finite differences on a staggered grid of 4th order in space and of 2nd order in time.

We apply our method to the M_w 6.3 Lesvos earthquake that occurred on June 12, 2017, 12:28 GMT, offshore the southeastern coast of the Greek island of Lesvos in the Lesvos Basin, Aegean Sea. According to the Geophysical Institute of the National Observatory of Athens (GI-NOA), it was a shallow crustal event with a hypocentral depth of 12.0 ± 1.7 km. The stress state in the area is characterized as transtensional, with minimum principal stress axis σ_3 oriented in the NNE-SSW direction (Konstantinou et al., 2017). The earthquake likely ruptured the eastern segment of the Lesvos Basin fault, oriented perpendicular to σ_3, dipping SSW with a normal faulting mechanism (Kiratzi, 2018). We show a map of the epicentral area in Fig. 3.2.

Based on the full-waveform centroid moment tensor (CMT) inversion performed before the dynamic inversion by the software ISOLA (Zahradník & Sokos, 2018), and summarized in the supplementary text of the thesis, we adopt the fault plane geometry and mechanism with strike/dip/rake values 113°/40°/-83°.

To assess model predictions of induced ground motion, we use data from 15 strong-motion stations of the Geodynamic Institute of the National Observatory of Athens (GI-NOA) and Bogazici University Kandilli Observatory and Earthquake Research Institute (KOERI) (Fig. 3.2). The records were tapered with a rectangular time window starting at the origin time of 2017/06/12 12:28:37 GMT and with a duration of 80 s, bandpass filtered between 0.05 and 0.15 Hz by the 4th order Butterworth filter, and integrated into displacements.

3.2 Results

A comparison of KDE estimates of 1-D marginal distributions of ρ_{pr}, ρ_0, ρ_1 and ρ_2 for model parameters (or parameters derived from them, such as a, ϕ, C_{ang} and C_{dist}) is shown in Fig. 3.3. The distributions for gross quantities that emerge as results of the forward computations, such as the seismic moment, radiation efficiency and ruptured area, are shown in Fig. 3.4. In Fig. 3.5 we plot the
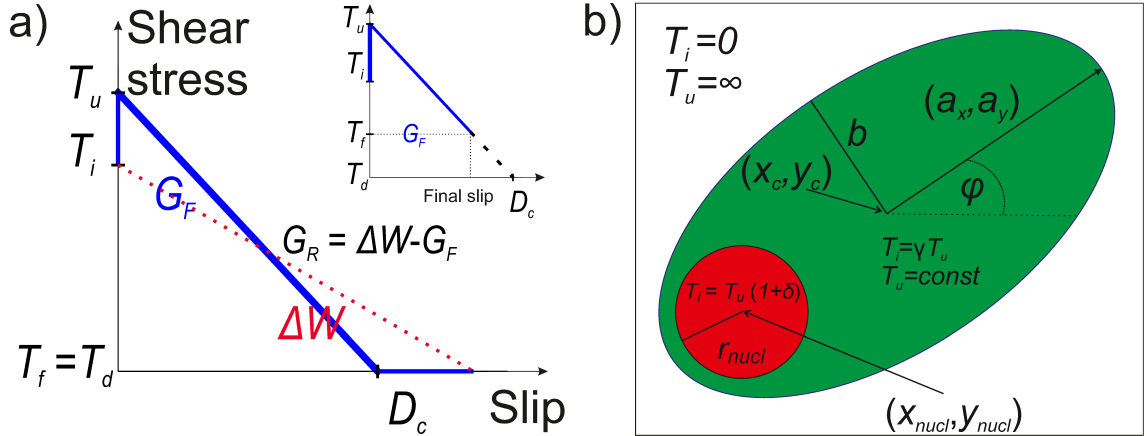
Figure 3.1: a) The linear slip weakening friction law. The magnitude of the shear stress at each point $\boldsymbol{x}$ on the fault has the initial value $T_i(\boldsymbol{x})$ (see Fig. b) and obeys linear elasticity until it is larger than or equal to T_u (yield strength). It then decreases linearly with accumulated slip (slip-path) $\mathfrak{s}$ until it reaches the final stress $T_f = T_d$ at $\mathfrak{s} = D_c$. The inset shows the case when slip stops before reaching D_c, in which case $T_f > T_d$. Stress drop is defined as $T_i - T_f$. The area ΔW under the red dotted line is the available strain energy surface density. The area G_F under the blue curve is the dissipated fracture energy surface density (energy dissipated from ΔW per area of rupture). The quantity $G_R = \Delta W - G_F$ is the radiated energy density. Integrals of these quantities over the fault plane are the available strain energy change ΔE, the dissipated fracture energy E_F, and radiated energy E_R, respectively. b) The elliptic parametrization used for the dynamic inversion. The yield strength T_u is finite and constant inside an elliptic patch and infinite elsewhere. The geometry of the ellipse is defined by the along-strike and along-dip coordinates of its center, x_c and y_c, the along-strike and along-dip components a_x and a_y of the semi-major axis, and the length of the semi-minor axis, b. The angle between the semi-major axis and the horizontal line is denoted by ϕ. The geometry of the nucleation zone (red) is parameterized by the coordinates of its center x_{nucl}, y_{nucl}, and the radius r_{nucl}. The magnitude of the shear stress inside the nucleation zone is defined relatively to T_u by the positive parameter δ: $T_i = T_u(1 + \delta)$. Elsewhere on the patch, T_i has a constant value of γT_u. Outside of the patch, it is zero. In the thesis, we transform some parameters to more illustrative quantities. In particular, instead of a_x and a_y, we show the quantities a and ϕ defined by the relations $a_x = a \cos \phi$, $a_y = a \sin \phi$, $\phi \in [0, \pi)$. Instead of x_c and y_c we show two derived quantities that characterize the connecting vector

$$\Delta \boldsymbol{r} = (x_c - x_{nucl}, y_c - y_{nucl}). \tag{3.4}$$

The first quantity, C_{dist}, is the length of $\Delta \boldsymbol{r}$ relative to the elliptic patch (equal to 0 when the nucleation is at the center of the patch and equal to 1 when it is at the boundary). Formally,

$$C_{dist} = \sqrt{\left(\frac{\Delta r'_x}{a}\right)^2 + \left(\frac{\Delta r'_y}{b}\right)^2}, \tag{3.5}$$

where $\Delta r'_x$ and $\Delta r'_y$ are the orthogonal projections of $\Delta \boldsymbol{r}$ on the semi-major and semi-minor axis, respectively. The second quantity, C_{ang}, is the angle between $\Delta \boldsymbol{r}$ and the horizontal axis:

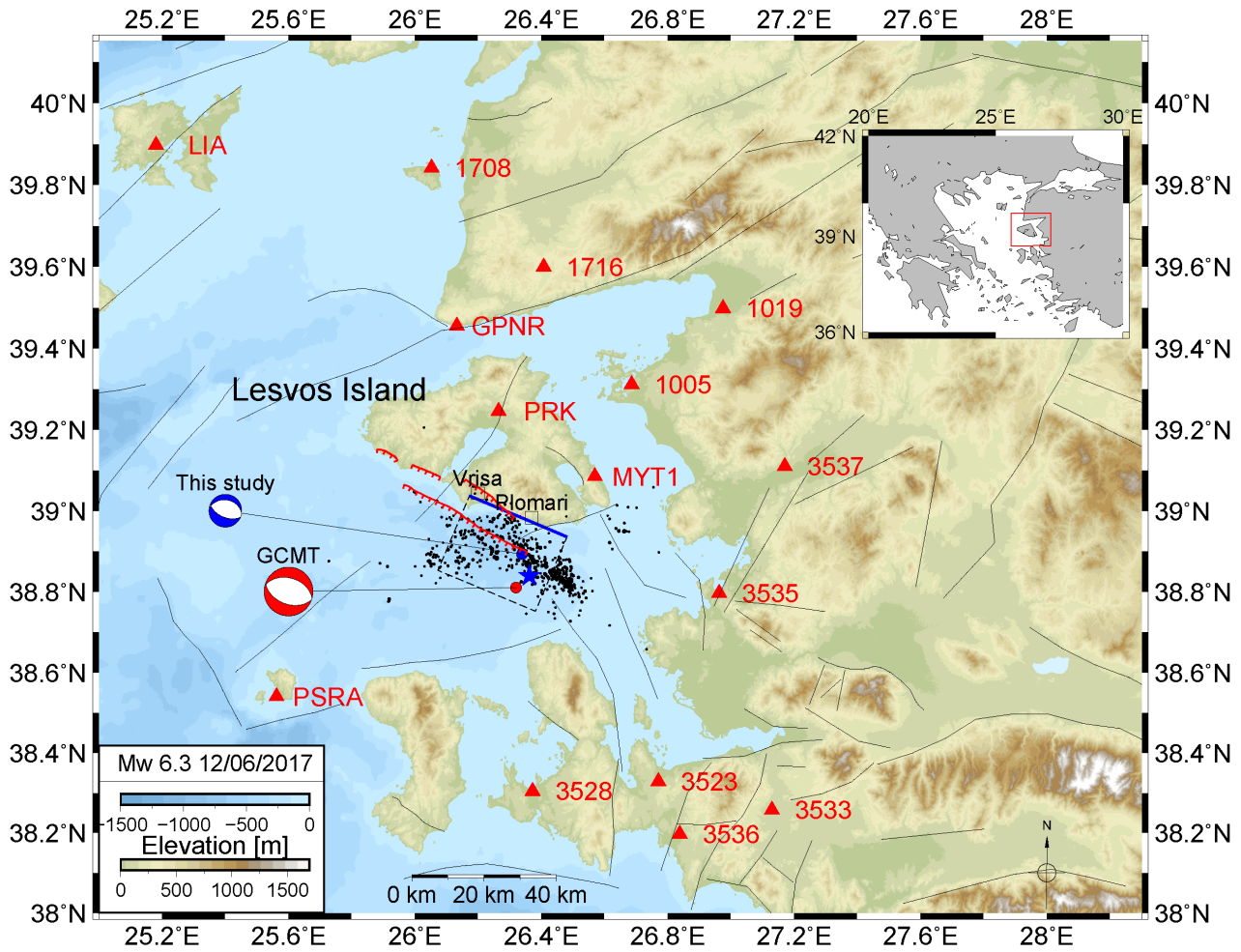$$C_{ang} = \mathrm{atan2}(\Delta r_y, \Delta r_x). \tag{3.6}$$

Figure 3.2: Map of the epicentral area of the 2017 M_w 6.3 Lesvos earthquake (see the inset for a wider geographic view). Strong-motion stations used for the dynamic inversion are shown as red triangles. The black rectangle shows the projection of the assumed fault plane used in the inversion. The blue solid line is the top fault edge at the surface. The blue beachball shows the centroid moment tensor of the M_w 6.3 mainshock inferred in this study, while the red beachball shows the GCMT centroid for the same event. Black dots are the aftershocks within two months after the event, as determined by GI-NOA. The hypocenter located by GI-NOA is denoted by a blue star. Fault traces from The European Database of Seismogenic Faults (EDSF; Basili et al., 2013) are shown as black lines. The red lines show inferred and mapped faults from Chatzipetros et al. (2013) and Ganas et al. (2013).

waveform fit of the best-fitting model along with KDE estimates of synthetic seismograms generated from samples of ρ_2.

Descriptions of the obtained distributions (including their 2-D versions and parameter correlations) and their interpretations are detailed in the thesis in sections 6.3 and 6.4. Briefly, we find that the final marginal posteriors ρ_2 of every model parameter are appreciably different from the prior distributions ρ_{pr}, with the minimum value of Hellinger distance $H_{pr,2}$ equal to 0.15 for parameter C_{dist} (see the black-and-blue numbers in Fig. 3.3). However, the update causing the biggest change varies among parameters. The quantities whose distributions are mainly affected by the rupture criterion (i.e., the greatest change happens in the $\rho_{pr} \rightarrow \rho_0$ transition, while the ρ_1 and ρ_2 distributions are very close to ρ_0) are δ and r_{nucl}. Parameters a and b are mostly constrained by the moment magnitude ($\rho_0 \rightarrow \rho_1$), as is the total ruptured area S_r. The distributions of the model parameters x_{nucl}, y_{nucl}, C_{ang} and γ, and certain emergent quantities, including the radiated energy, radiation efficiency, slip-weighted mean angle of propagation, stress drop, and rupture speed are mainly affected by seismograms ($\rho_1 \rightarrow \rho_2$). Finally, the distributions of parameters D_c and C_{dist} do not change very much in either transition, but the small changes accumulate and their ρ_2 distributions are appreciably different from ρ_{pr}.

The quantity best resolved by the seismogram information is the radiated energy, with its final posterior distribution ρ_2 peaking at 35 TJ and with 68% of values between 12 TJ and 65 TJ. Most models sampled from ρ_2 are characterized by slow mean rupture velocity (1.4-2.6 km/s), low radiation efficiency (10-40%), and low slip-weighted mean stress drop (2.2-6.5 MPa). The rupture is further characterized by pronounced nucleation and subshear propagation directed predominantly towards WNW.
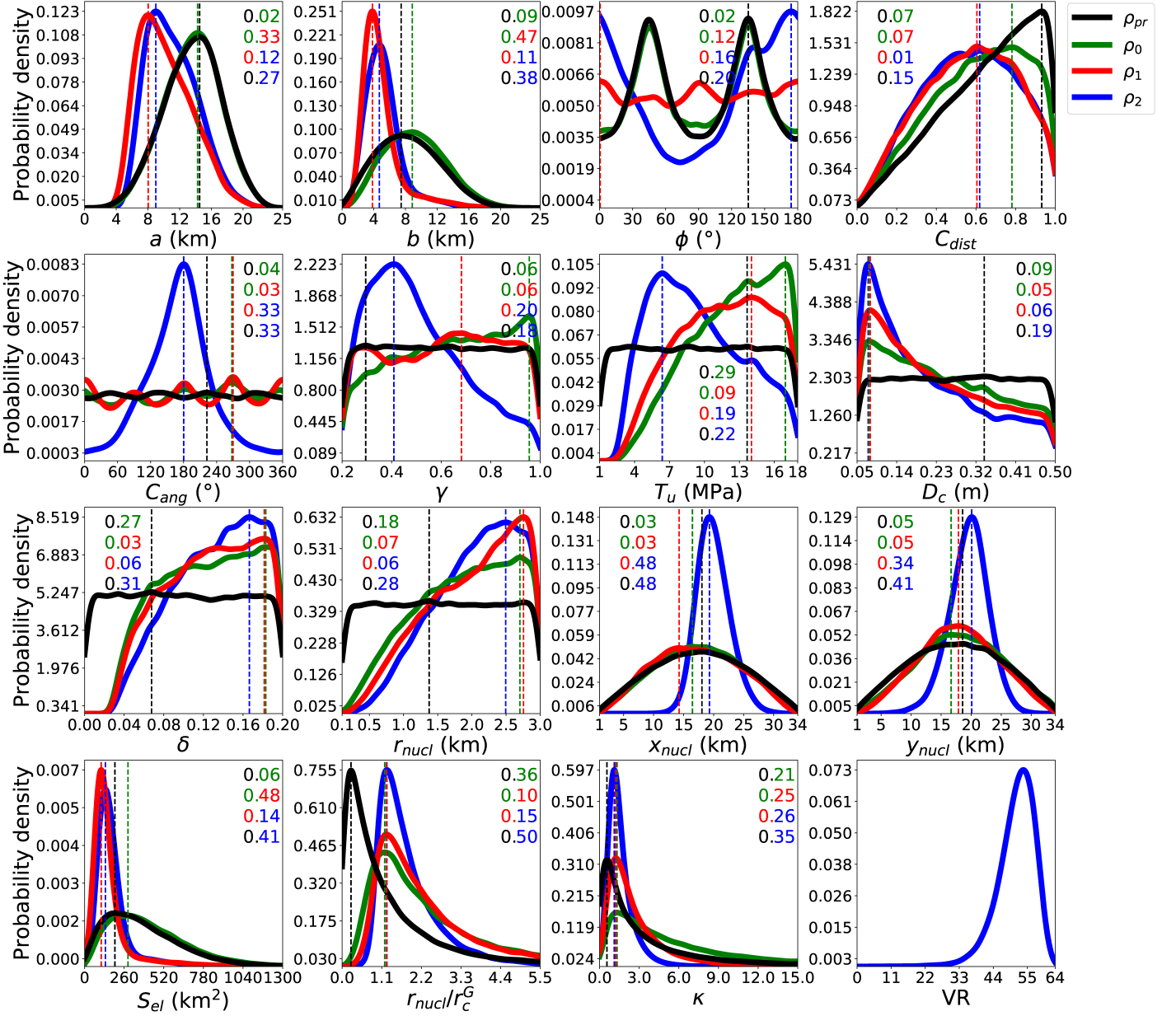
Figure 3.3: KDE estimates of 1-D marginal distributions for the model parameters and quantities derived from them, obtained with the Parallel Tempering algorithm. Different colors correspond to the prior distribution (ρ_{pr}) and posterior distributions incrementally constrained by the rupture condition (ρ_0), moment magnitude (ρ_1), and seismograms (ρ_2) (see legend). Vertical bars show the modes of each distribution. The numbers show the Hellinger distances between distributions, with color-coding representing the respective pair of distributions under comparison (for example, the distance between ρ_{pr} and ρ_0 is shown as a black-and-green number). Only the 12 parameters in the first three rows are independent, the quantities $S_{el} = \pi ab$, r_{nucl}/r_c^G (the ratio of the nucleation radius and an estimate of the minimal radius needed for rupture) and κ (so-called similarity parameter) were calculated from them. The KDE of seismogram variance reduction (VR) for samples of ρ_2 is shown at the bottom right.
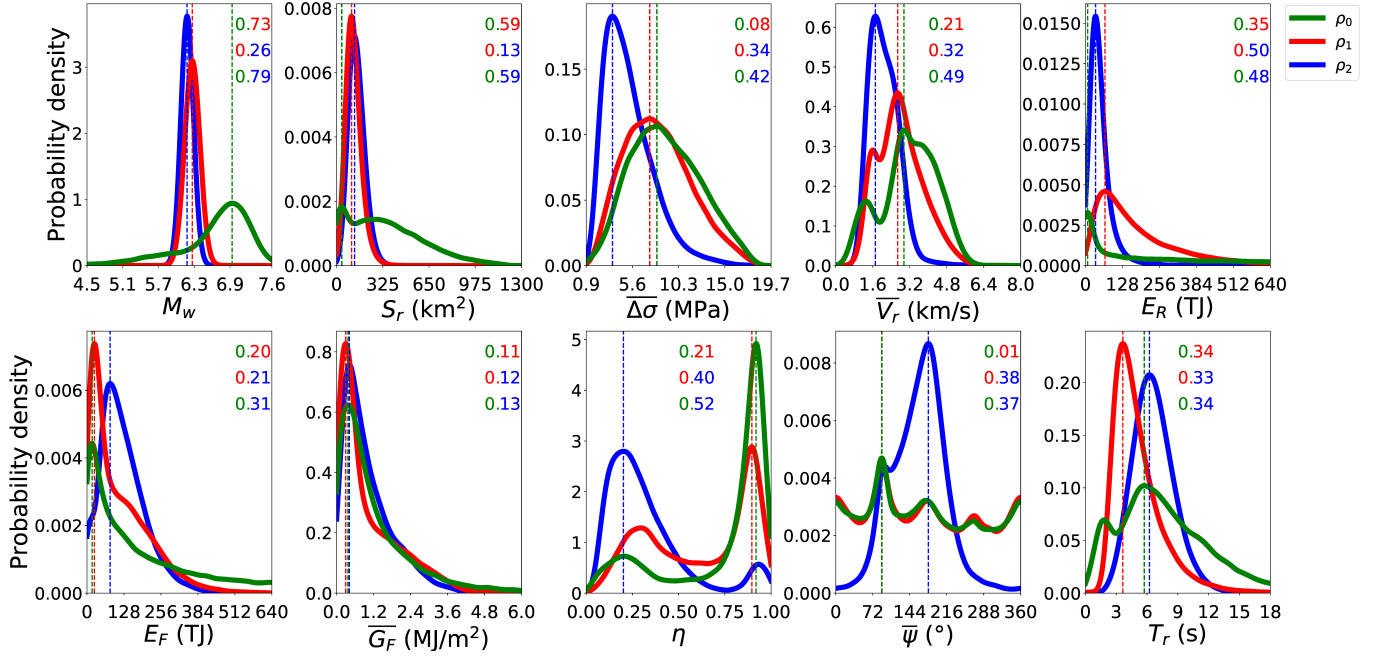
Figure 3.4: KDE estimates of 1-D marginal distributions for emergent quantities obtained with the Parallel Tempering algorithm. Different colors correspond to the posterior distributions incrementally constrained by the rupture condition (ρ_0), moment magnitude (ρ_1), and seismograms (ρ_2) (see legend). Vertical bars show the modes of each distribution. The numbers show the Hellinger distances between distributions, with color-coding representing the respective pair of distributions under comparison. M_w is the moment magnitude, S_r the ruptured area, $\overline{\Delta\sigma}$ the slip-weighted mean (SWM) stress drop, $\overline{V_r}$ the SWM rupture speed, E_r the radiated energy, E_F the dissipated energy, $\overline{G_F}$ is the area averaged E_F, η is the radiation efficiency, $\overline{\psi}$ the SWM rupture direction, and T_r is the effective duration of rupture.
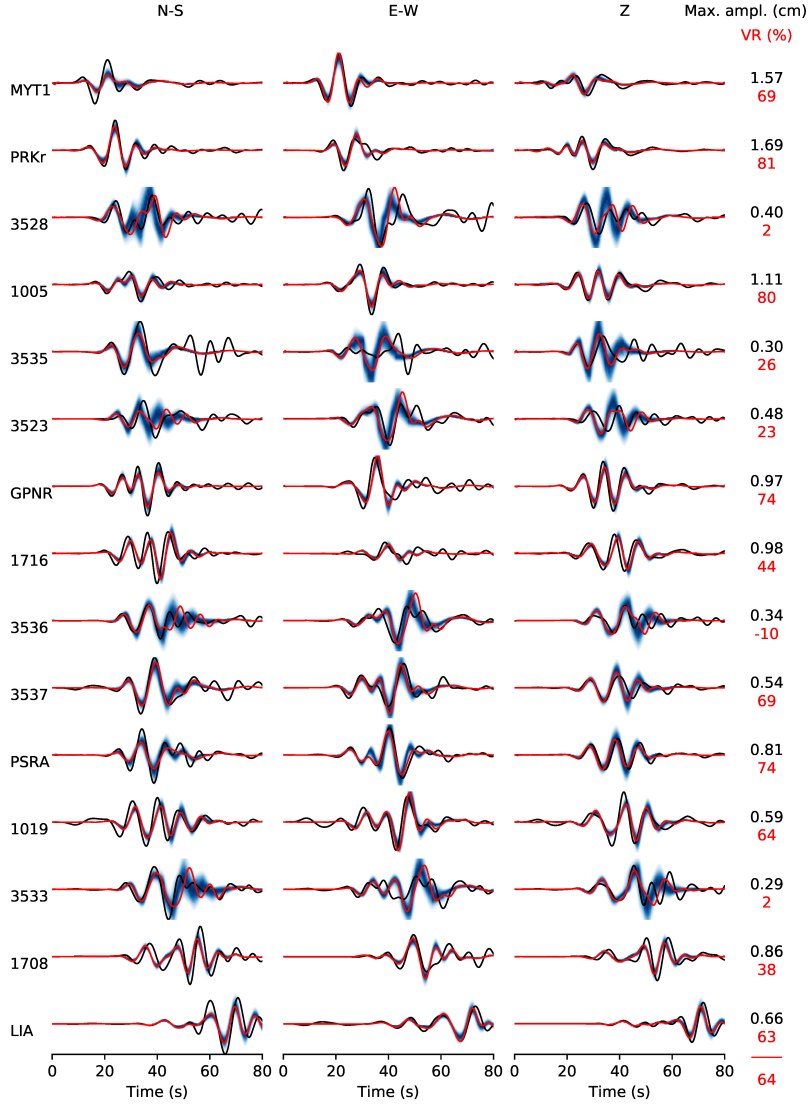
Figure 3.5: Displacement seismograms at the 15 selected stations in the frequency range of 0.05-0.15 Hz. Observed seismograms are black, synthetic seismograms of the best-fitting model are red. KDE estimates of synthetic seismogram posterior distribution, calculated at each time step, are blue. Numbers on the right show the maximum amplitude of the observed seismograms (black) and variance reduction (VR) at individual stations for the best-fitting model (red). Here, variance reduction is defined as:

$$\text{VR}\left(\boldsymbol{d(m)}, \boldsymbol{d}_{obs}\right) := 1 - \frac{||\boldsymbol{d(m)} - \boldsymbol{d}_{obs}||^2}{||\boldsymbol{d}_{obs}||^2}, \tag{3.7}$$

where $\boldsymbol{d(m)}$ is the vector of synthetic data produced by the model, $\boldsymbol{d_{obs}}$ are the observed data and $||\cdot||$ is the L_2 norm. The red number at the bottom is the overall VR of the best-fitting model. The time axis begins on 12 Jun 2017, 12:28:38.26 GMT.

Conclusions

The dissertation focuses on dynamic source modeling of tectonic earthquakes. We study the problem at both long (hundreds of years) and short (seconds) time scales. We use the rate-and-state friction law for the former case and the linear slip-weakening law for the latter case.

The first chapter describing the original research is focused on the influence of externally applied shear stress perturbations during simply periodic seismic cycles on the occurrence time of earthquakes. We examine this problem using the aging version of the rate-and-state law on finite strike-slip faults immersed in a 3-D homogeneous, isotropic elastic half-space, utilizing the quasi-dynamic approximation. We systematically study the dependence of the clock advance (the difference between earthquake occurrence times on the unperturbed and perturbed faults) on the application time of the stress load, its amplitude, and spatial extent, highlighting the importance of slip rate at the time and place of application.

For positive stress perturbations, the clock advance can be both positive and negative, while for negative change, it is only negative (clock delay). For a given amplitude and geometry of the stress perturbation, the graph of clock advance vs application time can be divided into three distinct parts (as also seen in previous studies, e.g., Perfettini et al. 2003; Gallovič 2008; Cho et al. 2009): the static phase, the oscillatory phase, and the instantaneous triggering phase.

During the static phase, which occurs at the beginning of the seismic cycle, the graph is constant, so the clock advance does not depend on the timing of the load. In the instantaneous triggering phase, which occurs near the end of the cycle and only for positive stress perturbations, the perturbation immediately destabilizes the whole fault and triggers an earthquake. In these two phases, the earthquakes following the perturbation are always whole system events, rupturing the whole fault.

The oscillatory phase, in which the clock advance graph is (non-periodically) increasing and decreasing, occurs in between the two phases. In the majority of the decreasing part of the oscillatory phase, whole system events are launched, as in the other two phases. But in a small portion of the decreasing part and in the increasing part, the earthquakes following the perturbation are only partial ruptures that do not completely release stress on the whole fault. The whole system earthquakes eventually get launched as well, but they are significantly delayed; the duration between large earthquakes may be prolonged by up to 80% when compared to the unperturbed cycles. This occurs even for positive perturbations, which normally tend to advance the upcoming earthquake.

We link this mechanism to the behavior observed on the Parkfield segment of the San-Andreas, California fault. This segment underwent quasi-periodic M_w 6 earthquakes with a mean recurrence time of 22 years and the next M_w 6 earthquake was expected to arrive between 1988 and 1993. Instead, it arrived in 2004, which corresponds to a significant delay. Moreover, the segment experienced a stress perturbation due to the 1983 Coalinga-Nuñez earthquakes and only smaller events (with M_w of at most 4.9) occurred on the segment in the expected period. We reproduce the mechanism described in the previous paragraph on a heterogeneous model of the Parkfield segment, adapted from Barbot et al. (2012), to demonstrate that it could have been responsible for the delay.

In the second chapter describing the original research, we present a Bayesian dynamic inversion for a 12-parameter elliptic model governed by the slip-weakening law, applied to the 2017 Lesvos M_w 6.3 Earthquake. Beginning with a prior probability density function (pdf) ρ_{pr} on the 12 parameters, we obtain three posterior pdfs by updating the prior with progressively more constraints on the model. To calculate the initial posterior pdf ρ_0, we use the constraint that the model results in a rupture that breaks at least twice the area of the nucleation zone and lasts more than 1 second. This condition removes uninteresting models that produce negligible wave radiation. As ρ_0 does not yet depend on seismic data, it may be understood as a corrected prior pdf. For the second pdf ρ_1, we require that the magnitude produced by the model is close to the value obtained from a prior centroid moment inversion. For the final pdf ρ_2, we add seismic waveforms from fifteen near-regional seismic stations and require that the model produces synthetic waveforms close to the observed ones.

We evaluate correlations and trade-offs of different pairs of parameters by examining their 2-D marginal pdfs. To quantify uncertainties for each parameter, we calculate the sizes of the highest density region (HDR) of the respective 1-D marginal pdfs. By comparing, for each quantity, the successive 1-D marginal pdfs for the chain $\rho_{pr} \rightarrow \rho_0 \rightarrow \rho_1 \rightarrow \rho_2$, we determine the step at which the quantity becomes the most resolved. We quantify this resolution by comparing the HDR sizes of successive distributions. We also evaluate the mutual dissimilarity of the pdfs by calculating the Hellinger distances between them.

We find that pdfs of some parameters either change only mildly in each update or significantly change only due to the first, minimum rupture, constraint. Therefore, neither the observed moment magnitude nor the waveforms are important for the shape of their final posterior (ρ_2) pdf. These parameters include the size of the nucleation zone, the initial stress (relative to the yield strength) inside the nucleation, the distance of the nucleation zone from the center of the patch, and the characteristic slip-weakening distance.

Pdfs of the dimensions of the patch and the total ruptured area are almost completely determined by adding the magnitude constraint — they changed only negligibly after adding the constraint on seismic waveforms.

Finally, we identify quantities strongly resolved by adding the waveform constraint. From model

parameters, these include the location of the hypocenter, its orientation with respect to the center of the patch, and the ratio of the initial stress to the yield strength. From quantities that emerge as results of the simulation, the best resolved was radiated energy, but a good resolution is also seen for the radiation efficiency, the mean angle of rupture propagation, and the slip-weighted average stress drop and rupture speed.

List of author's peer-reviewed publications

1. Kostka & Gallovič (2016): Kostka, F., and Gallovič, F. (2016), Static Coulomb stress load on a three-dimensional rate-and-state fault: Possible explanation of the anomalous delay of the 2004 Parkfield earthquake, J. Geophys. Res. Solid Earth, 121, 3517–3533, doi: 10.1002/2015JB012646 (1 impact journal citation not including self-citations).

2. Kostka et al. (2022): Kostka, F., Zahradník, J., Sokos, E. & Gallovič. F. (2022). Assessing the role of selected constraints in Bayesian dynamic source inversion: Application to the 2017 Mw 6.3 Lesvos earthquake, Geophys. J. Int., 228(1), 711–727, doi: 10.1093/gji/ggab359

Bibliography

Ampuero, J. P. & Ben-Zion, Y., 2008. Cracks, pulses and macroscopic asymmetry of dynamic rupture on a bimaterial interface with velocity-weakening friction, *Geophysical Journal International*, **173**.

Andrews, D. J., 1976a. Rupture velocity of plane strain shear cracks, *Journal of Geophysical Research (1896-1977)*, **81**(32), 5679–5687.

Andrews, D. J., 1976b. Rupture propagation with finite stress in antiplane strain, *Journal of Geophysical Research (1896-1977)*, **81**(20), 3575–3582.

Aochi, H. & Matsu'ura, M., 2002. Slip- and time-dependent fault constitutive law and its significance in earthquake generation cycles, *Pure and Applied Geophysics*, **159**, 2029–2044.

Aochi, H. & Ulrich, T., 2015. A probable earthquake scenario near Istanbul determined from dynamic simulations, *Bulletin of the Seismological Society of America*, **105**(3), 1468–1475.

Bakun, W. H., Aagaard, B., Dost, B., Ellsworth, W. L., Hardebeck, J. L., Harris, R. A., Ji, C., Johnston, M. J. S., Langbein, J., Lienkaemper, J. J., Michael, A. J., Murray, J. R., Nadeau, R. M., Reasenberg, P. A., Reichle, M. S., Roeloffs, E. A., Shakal, A., Simpson, R. W., & Waldhauser, F., 2005. Implications for prediction and hazard assessment from the 2004 Parkfield earthquake, *Nature*, **437**(7061), 969–974.

Barbot, S., Lapusta, N., & Avouac, J.-P., 2012. Under the hood of the earthquake machine: Toward predictive modeling of the seismic cycle, *Science*, **336**(6082), 707–710.

Basili, R., Kastelic, V., Demircioglu, M., B., Garcia, Moreno, D., Nemser, E., S., Petricca, P., Sboras, S., P., Besana-Ostman, G., M., Cabral, J., Camelbeeck, T., Caputo, R., Danciu, L., Domac, H., Fonseca, J., García-Mayordomo, J., Giardini, D., Glavatovic, B., Gulen, L., Ince, Y., Pavlides, S., Sesetyan, K., Tarabusi, G., Tiberti, M., M., Utkucu, M., Valensise, G., Vanneste, K., Vilanova, S., & Wössner, J., 2013. The European Database of Seismogenic Faults (EDSF) compiled in the framework of the project SHARE, *http://diss.rm.ingv.it/share-edsf/, doi: 10.6092/INGV.IT-SHARE-EDSF*.

Beeler, N. M., Tullis, T. E., & Weeks, J. D., 1994. The roles of time and displacement in the evolution effect in rock friction, *Geophysical Research Letters*, **21**, 1987–1990.

Ben-Zion, Y., Rice, J. R., & Dmowska, R., 1993. Interaction of the san andreas fault creeping segment with adjacent great rupture zones and earthquake recurrence at parkfield, *Journal of Geophysical Research: Solid Earth*, **98**(B2), 2135–2144.

Bizzarri, A., 2012. Modeling repeated slip failures on faults governed by slip-weakening friction, *The Bulletin of the Seismological Society of America*, **102**, 812–821.

Bizzarri, A., 2014. Rake rotation introduces ambiguity in the formulation of slip-dependent constitutive models: slip modulus or slip path?, *Annals of Geophysics*, **57**, 0547.

Bohloli, B., Soldal, M., Smith, H., Skurtveit, E., Choi, J. C., & Sauvin, G., 2020. Frictional Properties and Seismogenic Potential of Caprock Shales, *Energies*, **13**(23).

Burjánek, J. & Zahradník, J., 2007. Dynamic stress field of a kinematic earthquake source model with k-squared slip distribution, *Geophysical Journal International*, **171**(3), 1082–1097.

Chatzipetros, A., Kiratzi, A., Sboras, S., Zouros, N., & Pavlides, S., 2013. Active faulting in the north-eastern Aegean Sea Islands, *Tectonophysics*, **597-598**, 106–122.

Cho, I., Tada, T., & Kuwahara, Y., 2009. Stress triggering of large earthquakes complicated by transient aseismic slip episodes, *Journal of Geophysical Research: Solid Earth*, **114**(B7).

Di Carli, S., François-Holden, C., Peyrat, S., & Madariaga, R., 2010. Dynamic inversion of the 2000 tottori earthquake based on elliptical subfault approximations, *Journal of Geophysical Research: Solid Earth*, **115**(B12).

Dieterich, J. H., 1972. Time-dependent friction in rocks, *Journal of Geophysical Research*, **77**(20), 3690–3697.

Dieterich, J. H., 1979. Modeling of rock friction: 1. experimental results and constitutive equations, *Journal of Geophysical Research: Solid Earth*, **84**(B5), 2161–2168.

Díaz-Mojica, J., Cruz-Atienza, V. M., Madariaga, R., Singh, S. K., Tago, J., & Iglesias, A., 2014. Dynamic source inversion of the m6.5 intermediate-depth zumpango earthquake in central mexico: A parallel genetic algorithm, *Journal of Geophysical Research: Solid Earth*, **119**(10), 7768–7785.

Fukuyama, E. & Mikumo, T., 1993. Dynamic rupture analysis: Inversion for the source process of the 1990 Izu-Oshima, Japan, earthquake (M = 6.5), *Journal of Geophysical Research: Solid Earth*, **98**(B4), 6529–6542.

Gabriel, A.-A., Ampuero, J.-P., Dalguer, L. A., & Mai, P. M., 2012. The transition of dynamic rupture styles in elastic media under velocity-weakening friction, *Journal of Geophysical Research: Solid Earth*, **117**(B9).

Gallovič, F., 2008. Heterogeneous coulomb stress perturbation during earthquake cycles in a 3d rate-and-state fault model, *Geophysical Research Letters*, **35**(21).

Gallovič, F., Valentová, L., Ampuero, J.-P., & Gabriel, A.-A., 2019a. Bayesian dynamic finite-fault inversion: 1. Method and synthetic test, *Journal of Geophysical Research: Solid Earth*, **124**(7), 6949–6969.

Gallovič, F., Valentová, L., Ampuero, J.-P., & Gabriel, A.-A., 2019b. Bayesian Dynamic Finite-Fault Inversion: 2. Application to the 2016 Mw 6.2 Amatrice, Italy, earthquake, *Journal of Geophysical Research: Solid Earth*, **124**(7), 6970–6988.

Gallovič, F., Zahradník, J., Plicka, V., Sokos, E., Evangelidis, C., Fountoulakis, I., & Turhan, F., 2020. Complex rupture dynamics on an immature fault during the 2020 Mw 6.8 Elazığ earthquake, Turkey, *Communications Earth Environment*, **1**(1), 40.

Ganas, A., Oikonomou, I., & Tsimi, C., 2013. Noafaults: a digital database for active faults in greece, *Bull. Geol. Soc. Greece*, **47**, 518–530.

Herrera, C., Ruiz, S., Madariaga, R., & Poli, P., 2017. Dynamic inversion of the 2015 Jujuy earthquake and similarity with other intraslab events, *Geophysical Journal International*, **209**(2), 866–875.

Hirose, T., 2005. Growth of molten zone as a mechanism of slip weakening of simulated faults in gabbro during frictional melting, *Journal of Geophysical Research*, **110**(B5).

Ida, Y., 1972. Cohesive force across the tip of a longitudinal-shear crack and griffith's specific surface energy, *Journal of Geophysical Research (1896-1977)*, **77**(20), 3796–3805.

Ide, S. & Takeo, M., 1997. Determination of constitutive relations of fault slip based on seismic wave analysis, *Journal of Geophysical Research: Solid Earth*, **102**(B12), 27379–27391.

Kato, N., 2004. A possible effect of an intermediate depth intraslab earthquake on seismic cycles of interplate earthquakes at a subduction zone, *Earth, Planets and Space*, **56**(6), 553–561.

Kato, N. & Hirasawa, T., 2000. Effect of a large outer rise earthquake on seismic cycles of interplate earthquakes: A model study, *Journal of Geophysical Research: Solid Earth*, **105**(B1), 653–662.

Kiratzi, A., 2018. The 12 June 2017 Mw 6.3 Lesvos Island (Aegean Sea) earthquake: Slip model and directivity estimated with finite-fault inversion, *Tectonophysics*, **724-725**, 1–10.

Konstantinou, K. I., Mouslopoulou, V., Liang, W.-T., Heidbach, O., Oncken, O., & Suppe, J., 2017. Present-day crustal stress field in Greece inferred from regional-scale damped inversion of earthquake focal mechanisms, *Journal of Geophysical Research: Solid Earth*, **122**(1), 506–523.

Kostka, F. & Gallovič, F., 2016. Static Coulomb stress load on a three-dimensional rate-and-state fault: Possible explanation of the anomalous delay of the 2004 Parkfield earthquake, *Journal of Geophysical Research (Solid Earth)*, **121**(5), 3517–3533.

Kostka, F., Zahradník, J., Sokos, E., & Gallovič, F., 2022. Assessing the role of selected constraints in Bayesian dynamic source inversion: application to the 2017 Mw 6.3 Lesvos earthquake, *Geophysical Journal International*, **228**(1), 711–727.

Kuroki, H., Ito, H. M., & Yoshida, A., 2004. Effects of nearby large earthquakes on the occurrence time of the Tokai earthquake – An estimation based on a 3-D simulation of plate subduction –, *Earth, Planets and Space*, **56**(2), 169–178.

Liu, Y. & Rice, J. R., 2007. Spontaneous and triggered aseismic deformation transients in a subduction fault model, *Journal of Geophysical Research: Solid Earth*, **112**(B9).

Marone, C. & Saffer, D. M., 2015. The Mechanics of Frictional Healing and Slip Instability During the Seismic Cycle, in *Treatise on Geophysics: Earthquake Seismology*, pp. 111–138, Elsevier.

Marone, C., Raleigh, C. B., & Scholz, C. H., 1990. Frictional behavior and constitutive modeling of

simulated fault gouge, *Journal of Geophysical Research*, **95**(B5), 7007.

Martinec, Z., 2019. *Principles of Continuum Mechanics: A Basic Course for Physicists*, Nečas Center Series, Springer International Publishing; Birkhäuser, 1st edn.

McGarr, A., 2003. Maximum slip in earthquake fault zones, apparent stress, and stick-slip friction, *Bulletin of the Seismological Society of America*, **93**(6), 2355–2362.

Mirwald, A., Cruz-Atienza, V. M., Díaz-Mojica, J., Iglesias, A., Singh, S. K., Villafuerte, C., & Tago, J., 2019. The 19 September 2017 (Mw 7.1) Intermediate-Depth Mexican Earthquake: A Slow and Energetically Inefficient Deadly Shock, *Geophysical Research Letters*, **46**(4), 2054–2064.

Nadeau, R. M. & McEvilly, T. V., 1999. Fault Slip Rates at Depth from Recurrence Intervals of Repeating Microearthquakes, *Science*, **285**(5428), 718–721.

Nadeau, R. M. & McEvilly, T. V., 2004. Periodic Pulsing of Characteristic Microearthquakes on the San Andreas Fault, *Science*, **303**(5655), 220–222.

Ohnaka, M., 2013. *The Physics of Rock Failure and Earthquakes*, Cambridge University Press, Cambridge.

Okada, Y., 1992. Internal deformation due to shear and tensile faults in a half-space, *Bulletin of the Seismological Society of America*, **82**(2), 1018–1040.

Perfettini, H., Schmittbuhl, J., & Cochard, A., 2003. Shear and normal load perturbations on a two-dimensional continuous fault: 1. Static triggering, *Journal of Geophysical Research*, **108**, 2408.

Peyrat, S. & Olsen, K. B., 2004. Nonlinear dynamic rupture inversion of the 2000 Western Tottori, Japan, earthquake, *Geophysical Research Letters*, **31**(5).

Peyrat, S., Olsen, K., & Madariaga, R., 2001. Dynamic modeling of the 1992 Landers earthquake, *Journal of Geophysical Research*, **106**(B11), 26,467–26,482.

Premus, J., Gallovič, F., & Hanyk Ladislav. Gabriel, A. A., 2020. FD3D_TSN: A fast and simple code for dynamic rupture simulations with GPU acceleration, *Seismological Research Letters*, **91**(5), 2881–2889.

Pulido, N. & Irikura, K., 2000. Estimation of dynamic rupture parameters from the radiated seismic energy and apparent stress, *Geophysical Research Letters*, **27**(23), 3945–3948.

Rice, J. R., 1993. Spatio-temporal complexity of slip on a fault, *Journal of Geophysical Research: Solid Earth*, **98**(B6), 9885–9907.

Ruina, A., 1980. *Friction Laws and Instabilities: A Quasistatic Analysis of Some Dry Frictional Behavior*, Division of Engineering, Brown University.

Ruina, A., 1983. Slip instability and state variable friction laws, *Journal of Geophysical Research: Solid Earth*, **88**(B12), 10359–10370.

Ruiz, S. & Madariaga, R., 2011. Determination of the friction law parameters of the Mw 6.7 Michilla earthquake in northern Chile by dynamic inversion, *Geophys. Res. Lett.*, **38**(9).

Ruiz, S. & Madariaga, R., 2013. Kinematic and Dynamic Inversion of the 2008 Northern Iwate

Earthquake, *Bulletin of the Seismological Society of America*, **103**(2A), 694–708.

Sambridge, M., 2013. A Parallel Tempering algorithm for probabilistic sampling and multimodal optimization, *Geophysical Journal International*, **196**(1), 357–374.

Shemyakin, A., 2014. Hellinger Distance and Non-informative Priors, *Bayesian Analysis*, **9**(4), 923 – 938.

Stirling, M. W., Wesnousky, S. G., & Shimazaki, K., 1996. Fault trace complexity, cumulative slip, and the shape of the magnitude-frequency distribution for strike-slip faults: a global survey, *Geophysical Journal International*, **124**(3), 833–868.

Swendsen, R. H. & Wang, J.-S., 1986. Replica Monte Carlo Simulation of Spin-Glasses, *Phys. Rev. Lett.*, **57**, 2607–2609.

Tinti, E., Spudich, P., & Cocco, M., 2005. Earthquake fracture energy inferred from kinematic rupture models on extended faults, *J. Geophys. Res.*, **110**(B12).

Twardzik, C., Das, S., & Madariaga, R., 2014. Inversion for the physical parameters that control the source dynamics of the 2004 Parkfield earthquake, *Journal of Geophysical Research: Solid Earth*, **119**(9), 7010–7027.

Wesnousky, S. G., 1994. The Gutenberg-Richter or characteristic earthquake distribution, which is it?, *Bulletin of the Seismological Society of America*, **84**(6), 1940–1959.

Zahradník, J. & Sokos, E., 2018. *ISOLA Code for Multiple-Point Source Modeling—Review*, pp. 1–28, Springer International Publishing, Cham.

Zambom, A. Z. & Dias, R., 2013. A Review of Kernel Density Estimation with Applications to Econometrics, *International Econometric Review (IER)*, **5**(1), 20–42.

Zelst, I., Wollherr, S., Gabriel, A., Madden, E., & Dinther, Y., 2019. Modeling megathrust earthquakes across scales: One-way coupling from geodynamics and seismic cycles to dynamic rupture, *Journal of Geophysical Research: Solid Earth*, **124**.